

Neurophysiological stratification of major depressive disorder by distinct trajectories

Received: 9 February 2023

Accepted: 13 September 2023

Published online: 23 October 2023


 Check for updates

Di Chen ^{1,2,13}, Xiang Wang^{3,4,5,13}, Valerie Voon^{1,2,6,13}, Yuchao Jiang ^{1,2}, Chun-Yi Zac Lo ^{1,2}, Linbo Wang^{1,2}, Chun Shen^{1,2}, Shitong Xiang ^{1,2}, Shuqiao Yao³, Jie Zhang^{1,2}, ZIB Consortium*, DIRECT Consortium*, Tianye Jia ^{1,2,7} , Wei Cheng ^{1,2,8,9,10,11}  & Jianfeng Feng ^{1,2,12} 

Major depressive disorder (MDD) has been characterized by structural abnormalities of multiple brain regions. Nevertheless, little is known about the underlying neuropathological origin of MDD, particularly based on distinct trajectories of brain atrophy. Here, using the data-driven subtype and stage inference algorithm on large case–control magnetic resonance imaging data from 3,940 individuals (1,789 patients with MDD; 2,151 healthy controls), we demonstrated three highly robust spatiotemporal MDD subtypes: subtype 1 initiates from the subgenual anterior cingulate cortex, subtype 2 starts at the hippocampus and subtype 3 begins in the superior frontal gyrus and then the orbitofrontal cortex. These subtypes also exhibited distinct clinical profiles and differing transcriptomic gene expressions. Specifically, we identified suicide risk as the characteristic symptom for the ‘anterior cingulate cortex-led’ subtype, as well as low motivation (for example, work interests) for the ‘frontal-led’ and somatic anxiety for the ‘hippocampus-led’. Distinguishable cell type-specific transcriptional signatures further indicate distinct origins of MDD subtypes. Together, our data-driven findings demonstrate different spatiotemporal trajectories of MDD subtypes, which may contribute to the potential for individualized diagnostics, suicide risk alerts and optimizing therapeutic targeting.

Major depressive disorder (MDD) is a common major public health issue and a global leading cause of disability¹. Behavioural symptoms such as feelings of sadness and helplessness, loss of pleasure and lack of motivation and cognitive deficits are key features of MDD^{2,3}. The diagnosis of MDD is guided by subjective behavioural

symptoms rather than objective indices with remarkable heterogeneity in phenotypic presentation, aetiology and longitudinal trajectory^{4–6}. Emerging consensus suggests MDD may consist of multiple subtypes^{4,7,8}. However, few studies have managed to demonstrate whether highly reproducible neuropathological features, such as

¹Institute of Science and Technology for Brain-Inspired Intelligence, Fudan University, Shanghai, China. ²Key Laboratory of Computational Neuroscience and Brain-Inspired Intelligence (Fudan University), Ministry of Education, Shanghai, China. ³Medical Psychological Center, The Second Xiangya Hospital, Central South University, Changsha, China. ⁴Medical Psychological Institute, Central South University, Changsha, China. ⁵China National Clinical Research Center on Mental Disorders (Xiangya), Changsha, China. ⁶Department of Psychiatry, University of Cambridge, Cambridge, UK. ⁷Institute of Psychiatry, Psychology & Neuroscience, SGDP Centre, King’s College London, London, UK. ⁸Department of Neurology, Huashan Hospital, Fudan University, Shanghai, China. ⁹Fudan ISTBI—ZJNU Algorithm Centre for Brain-Inspired Intelligence, Zhejiang Normal University, Jinhua, China. ¹⁰Shanghai Medical College and Zhongshan Hospital Immunotherapy Technology Transfer Center, Shanghai, China. ¹¹MOE Frontiers Center for Brain Science, Fudan University, Shanghai, China. ¹²Department of Computer Science, University of Warwick, Coventry, UK. ¹³These authors contributed equally: Di Chen, Xiang Wang, Valerie Voon. *Lists of authors and their affiliations appear at the end of the paper.  e-mail: tianyejia@fudan.edu.cn; wcheng@fudan.edu.cn; jffeng@fudan.edu.cn

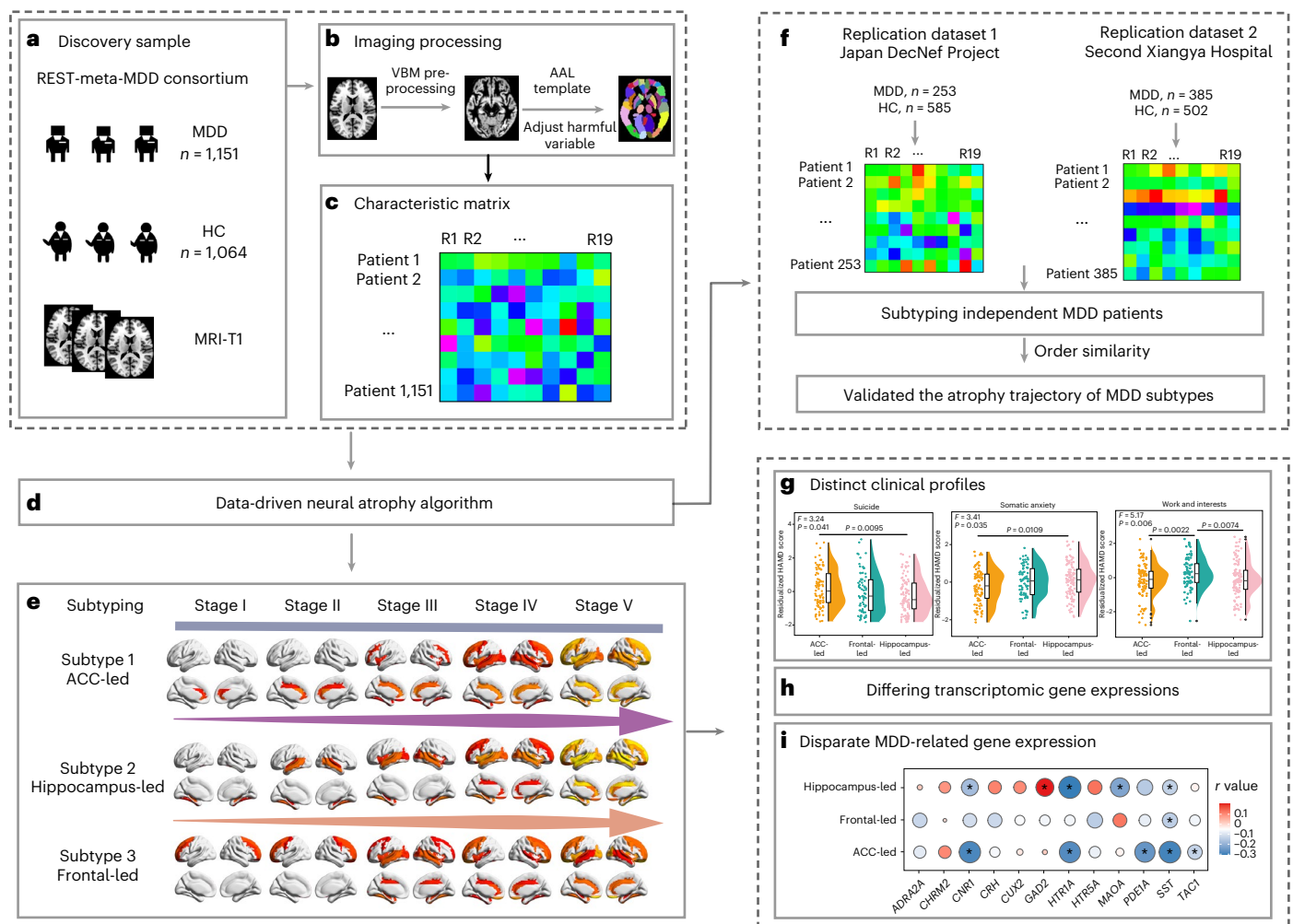


Fig. 1 | Schematic overview of the present study. This schematic overview provides a visual representation of the framework for the present study. The discovery samples from the REST-meta-MDD (a), image processing procedures (b), characteristic matrix of the brain images (c), application of the data-driven

neural atrophy algorithm (d), identification of topological subtypes of MDD (e), evaluation of the robustness of MDD subtypes (f), characterization of MDD subtypes by clinical profiles (g), differing transcriptomic gene expressions (h), disparate MDD-related gene expression (i).

distinct progressive anatomical brain atrophy, could underlie different MDD subtypes.

Recent developments in magnetic resonance imaging (MRI) provide insights into the potential for neural biomarkers to characterize mental disorders to distinguish patients from healthy controls (HCs)^{3,9–12}. From the large-scale Enhancing NeuroImaging Genetics through Meta-Analysis consortium, patients with MDD show reduced volume of the hippocampus¹¹ and lower cortical thickness in the anterior cingulate cortex (ACC), orbitofrontal cortex (OFC), insula, fusiform gyrus, superior frontal gyrus (SFG) and temporal lobe^{13–16}. Mid cingulate structural findings are also functionally associated with the experience of negative affect and pain in MDD¹⁷. Previous functional MRI studies further identified OFC, hippocampus, ACC, insula, middle frontal gyrus and rectus regions as enriched hubs that distinguish MDD from HCs^{5,18–21}.

Beyond the simple categorization of pathological versus healthy groups, studies have also explored the use of neuroanatomical (grey matter density) features to identify subtype of MDD^{7,22}. Most notably, the subtype and stage inference (SuStaln) algorithm in neuroscience has provided insights into how differing mechanisms underlying volumetric changes and anatomical atrophy might result in heterogeneous clinical presentations of mental disorders^{23–25}.

The SuStaln model is based on the Bayesian inversion of a generative model of disease progression²³. This model assumes the existence of an unknown number of subtypes, each characterized by distinct progressive patterns of disease biomarkers, specifically changes in grey matter density over the brain. These ‘trajectories’ are represented as ordered sequences of progressive biomarker changes corresponding to different disease stages²³. To generate a sample from this model, a specific subtype and stage are selected to produce a pattern of biomarkers. Importantly, this approach allows for the reconstruction of ‘trajectories’ for each subtype using cross-sectional data, by identifying the best subgroup and disease stage for each subject. Through model inversion, it becomes possible to assign a probability to each subject indicating their likelihood of belonging to a particular subgroup and stage of disease progression. By effectively disentangling the subtype and stage, this generative model inversion uncovers the underlying causes of measurable pathology. The inversion process of this generative model employs standard procedures such as expectation maximization and Markov chain Monte Carlo²³. Using the SuStaln model, based on cross-sectional samples, we focus on characterizing anatomical volumetric changes contributing to heterogeneity, particularly on predicted ‘trajectory’ (that is, the most probable sequence of spatial progression) that contributes to grey matter atrophy.

In this Article, we applied the SuStaln algorithm to grey matter volume (GMV), as characterized by voxel-based morphometry, in a large neuroimaging cohort (that is, $n_{\text{MDD}} = 1,151$, $n_{\text{HC}} = 1,064$) of the REST-meta-MDD project^{10,26}. Using Bayesian model selection, we identified the number of subtypes and validated the associated patterns of atrophy in two replication studies ($n_{\text{MDD}} = 253$, $n_{\text{HC}} = 585$ for the DecNef Project from Japan²⁷; $n_{\text{MDD}} = 385$, $n_{\text{HC}} = 502$ from the Second Xiangya Hospital project). Having established the predictive validity of the model, we then present a series of construct validations by showing notable correlations with clinical phenotypes. To investigate different potential genetic factors of MDD subtypes, we also employed the Allen Human Brain Atlas (AHBA) microarray dataset (<http://human.brain-map.org>), which has been used to identify transcriptomics associated with the pattern of specific disease progression²⁸. Figure 1 provides an overview of this present study.

Results

Whole-brain analysis of brain GMV

We first identified the most distinguishable brain patterns between MDD and healthy controls through GMV using a whole-brain analysis approach. Using the Automated Anatomical Labeling Atlas (AAL)-2 brain template, we identified whole-brain region of interest (ROI)-based differences (Fig. 2a) after controlling for factors including total intracranial volume (TIV), age, sex, years of education and site in the REST-meta-MDD project ($n_{\text{MDD}} = 1,151$, $n_{\text{HC}} = 1,064$; Supplementary Table 1); for details, see Supplementary Table 2.

Using the replication dataset from the Japan DecNef Project ($n_{\text{MDD}} = 253$, $n_{\text{HC}} = 585$; Supplementary Table 1), we also confirmed this MDD brain pattern using the same whole-brain ROI-based analysis procedure (Supplementary Fig. 1 and Supplementary Table 3). We observed a significant correlation of ROI-based brain pattern differences (that is, case-control t values) between the REST-meta-MDD project and the Japan DecNef Project (Spearman $r = 0.44$, $P_{\text{permu}} = 0.002$ after 10,000 times of standard permutation flow; Supplementary Fig. 2), thus confirming the consistency of the identified MDD brain pattern. In the second replication cohort from the Second Xiangya Hospital, however, we did not observe a significant pattern similarity ($P = 0.7856$) with the discovery data. This is probably due to a much younger age in the second replication cohort (mean age 22.21 years, standard deviation (s.d.) 5.22 years; $n_{\text{MDD}} = 385$, $n_{\text{HC}} = 502$) in contrast with the discovery dataset (mean age 36.80 years, s.d. 15.08 years; $n_{\text{MDD}} = 1,151$, $n_{\text{HC}} = 1,064$). Indeed, after partitioning the second replication cohort individuals into adolescents (age <21 years) and adults (age ≥ 21 years) (that is, adolescents: age <21 years, $n_{\text{MDD}} = 173$, $n_{\text{HC}} = 277$, mean age 18.92 years, s.d. 1.13 years; adults: age ≥ 21 years, $n_{\text{MDD}} = 212$, $n_{\text{HC}} = 225$, mean age 25.60 years, s.d. 5.60 years), we found that the adult group (Spearman $r_{\text{adults}} = 0.18$) had a significantly higher similarity with the discovery datasets than the adolescent group (Spearman $r = -0.16$) ($r_{\text{dif}} = 0.34$, $P_{\text{permu}} = 0.0454$ based on 10,000 times permutation).

Identification of topological subtype of MDD

We then applied the SuStaln algorithm to identify distinct sustained brain atrophy throughout all progressive stages, that is, the ‘trajectories’²⁵, from 2,215 individuals ($n_{\text{MDD}} = 1,151$, $n_{\text{HC}} = 1,064$; Supplementary

Table 1) of the REST-meta-MDD project. Due to the distribution of average negative log-likelihood from five-fold validation, a three-cluster partition was the optimal choice (for details, see Methods), which showed the minimum cross-validation information criterion (CVIC) (Supplementary Fig. 3a) and maximal log-likelihood (Supplementary Fig. 3b). The following three MDD subtypes with distinct ‘trajectories’ were identified from the SuStaln model: subtype 1 showed initial atrophy starting in the subgenual ACC, then progressing to the supracallosal ACC, to the pregenual ACC and finally to the middle cingulate gyri (Fig. 2b). Subtype 2 exhibited atrophy starting in the hippocampus, then progressing to temporal regions and the fusiform gyrus (Fig. 2b). Subtype 3 displayed atrophy beginning in the SFG, then progressing to the middle frontal gyrus and ultimately to the OFC (Fig. 2b).

The SuStaln algorithm assigned each patient with MDD of the REST-meta-MDD project ($n_{\text{MDD}} = 1,151$; Fig. 2c) to the most probable subtype label and atrophy stage. Note that patients with MDD in ‘stage 0’ in the atrophy stage were identified as ‘pre-atrophy’, while other patients were defined as ‘post-atrophy’ in the present study. A total of 433 patients with MDD (37.62% of the total) were classified as subtype 1, which was further divided into ‘pre-atrophy’ ($n_{\text{pre}} = 187$ for subtype 1) or ‘post-atrophy’ (that is, ‘ACC-led’; $n_{\text{ACC}} = 246$) phase. The subtype 2 patients with MDD ($n_{\text{subtype2}} = 486$, 42.22% of the total) were also assigned to ‘pre-atrophy’ ($n_{\text{pre}} = 249$ for subtype 2) or ‘post-atrophy’ (that is, ‘hippocampus-led’, $n_{\text{hippocampus}} = 237$) phase, as well as the subtype 3 ($n_{\text{subtype3}} = 232$, 20.16% of the total; $n_{\text{pre}} = 72$ for subtype 3, $n_{\text{frontal}} = 160$). The probability-based distribution of three post-atrophy ‘trajectories’ (that is, ‘ACC-led’, ‘hippocampus-led’ and ‘frontal-led’) from the REST-meta-MDD project can be found in Fig. 2d. We then investigated the influence of confounders (that is, medication history, age, sex and education) on MDD subtypes and found no potential impact (Supplementary Table 4 and Supplementary Fig. 4).

To further characterize the stage-based progression of atrophy for patients with MDD from the REST-meta-MDD project, we calculated the mean z -value images (that is, reduction of GMV) and investigated their relationship with SuStaln stage. The decrease of ROI-based GMV (that is, increasing z -value) for each subtype (that is, ‘post-atrophy’) is shown in Fig. 2e. In addition, reduced total GMV ($r = -0.29$, $P_{\text{Bonferroni}} < 0.001$, Bonferroni corrected; Fig. 2f), increased cerebrospinal fluid (CSF) ($r = 0.56$, $P_{\text{Bonferroni}} < 0.001$, Bonferroni corrected; Fig. 2g), and a trend towards larger white matter volume (WMV) were also observed with increased SuStaln stages ($r = 0.07$, $P_{\text{Bonferroni}} = 0.066$, Bonferroni corrected; Fig. 2h).

We then investigated the relationship between ROI-based GMV (z -value) and SuStaln stage. As expected, we observed the z -valued GMV of ACC significantly correlated with the SuStaln stage in the ‘ACC-led’ subtype ($r = 0.11$, $P_{\text{FDR}} = 0.048$ for subgenual ACC; $r = 0.52$, $P_{\text{FDR}} < 0.001$ for pregenual ACC; $r = 0.36$, $P_{\text{FDR}} < 0.001$ for supracallosal ACC; false discovery rate (FDR) corrected). The GMV of the hippocampus (z -value) was also associated with the SuStaln stage in the ‘hippocampus-led’ subtype ($r = 0.26$, $P_{\text{FDR}} < 0.001$; FDR corrected). A significant correlation of the ‘frontal-led’ subtype was similarly found in OFC ($r = 0.58$, $P_{\text{FDR}} < 0.001$ for medial OFC; $r = 0.44$,

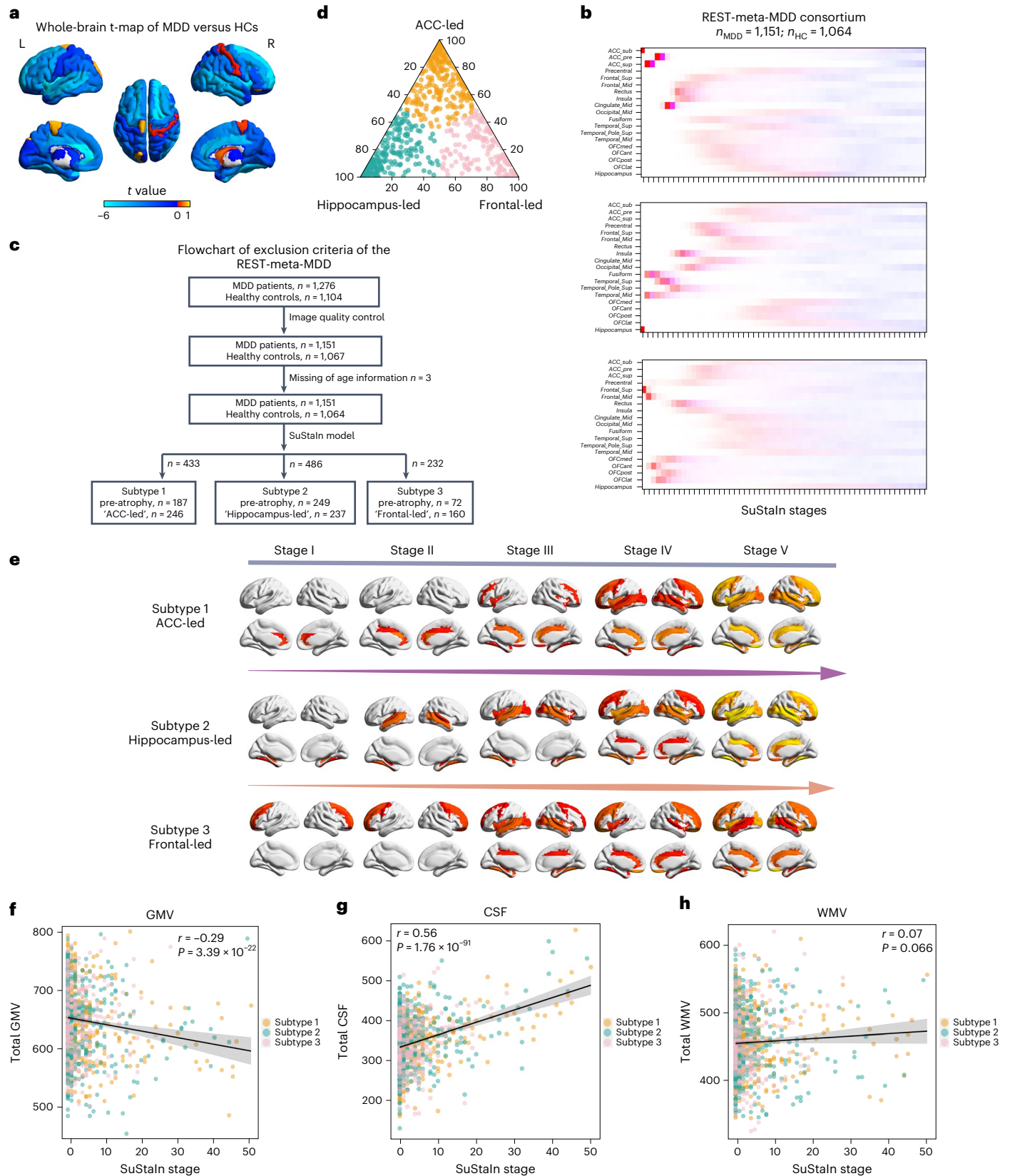
Fig. 2 | Identified topological subtype of MDD from the REST-meta-MDD project. **a**, ROI-based group differences of the REST-meta-MDD project in GMV between patients with MDD and HCs. L, left. R, right. **b**, Three atrophy ‘trajectories’ in the REST-meta-MDD project. The positional variance diagrams employ various colours to depict the probability of each brain region attaining a specific z -score, providing a visual representation of the variability in position across different regions. Different colours shown on the visualization correspond with varying degrees of GMV loss severity. Mildly affected regions are depicted as red ($z = 1$), moderately affected regions appear as magenta ($z = 1.5$) and severely affected regions are represented by blue ($z = 2$). The colour density illustrates the

proportion of the posterior distribution that events arise in a particular position in the sequence^{23,25}. **c**, Flowchart of exclusion criteria of the REST-meta-MDD project. **d**, The probability-based distribution of three post-atrophy (that is, ACC-led, hippocampus-led and frontal-led). **e**, Decrease of ROI-based GMV (that is, increasing z -value) for each ‘post-atrophy’. Stage I: stage = 1, stage II: $2 \leq \text{stage} \leq 3$, stage III: $4 \leq \text{stage} \leq 7$, stage IV: $8 \leq \text{stage} \leq 15$, stage V: $16 \leq \text{stage}$. **f–h**, Associations between total brain (that is, GMV (**f**), CSF (**g**) and WMV (**h**)) and SuStaln stage. Pearson correlation test (two-tailed P value, Bonferroni corrected) was used. The error band represents the 95% confidence interval around the line.

$P_{FDR} < 0.001$ for anterior OFC; $r = 0.38$, $P_{FDR} < 0.001$ for posterior OFC; $r = 0.57$, $P_{FDR} < 0.001$ for lateral OFC; FDR corrected), but not in the SFG ($r = 0.08$, $P_{FDR} = 0.158$; FDR corrected).

We further investigated the stability of the SuStaln ‘trajectories’ with additional z-score thresholds (that is, $z = [1, 2, 3]$ from previous

SuStaln publications^{23,25} and a further increased $z = [2, 3, 4]$) and found consistent results (Supplementary Fig. 5). Further, the SuStaln model with a small number ($n = 14$) of ROIs (that is, merged temporal and OFC areas, respectively) also showed similar ‘trajectories’ (Supplementary Fig. 6).



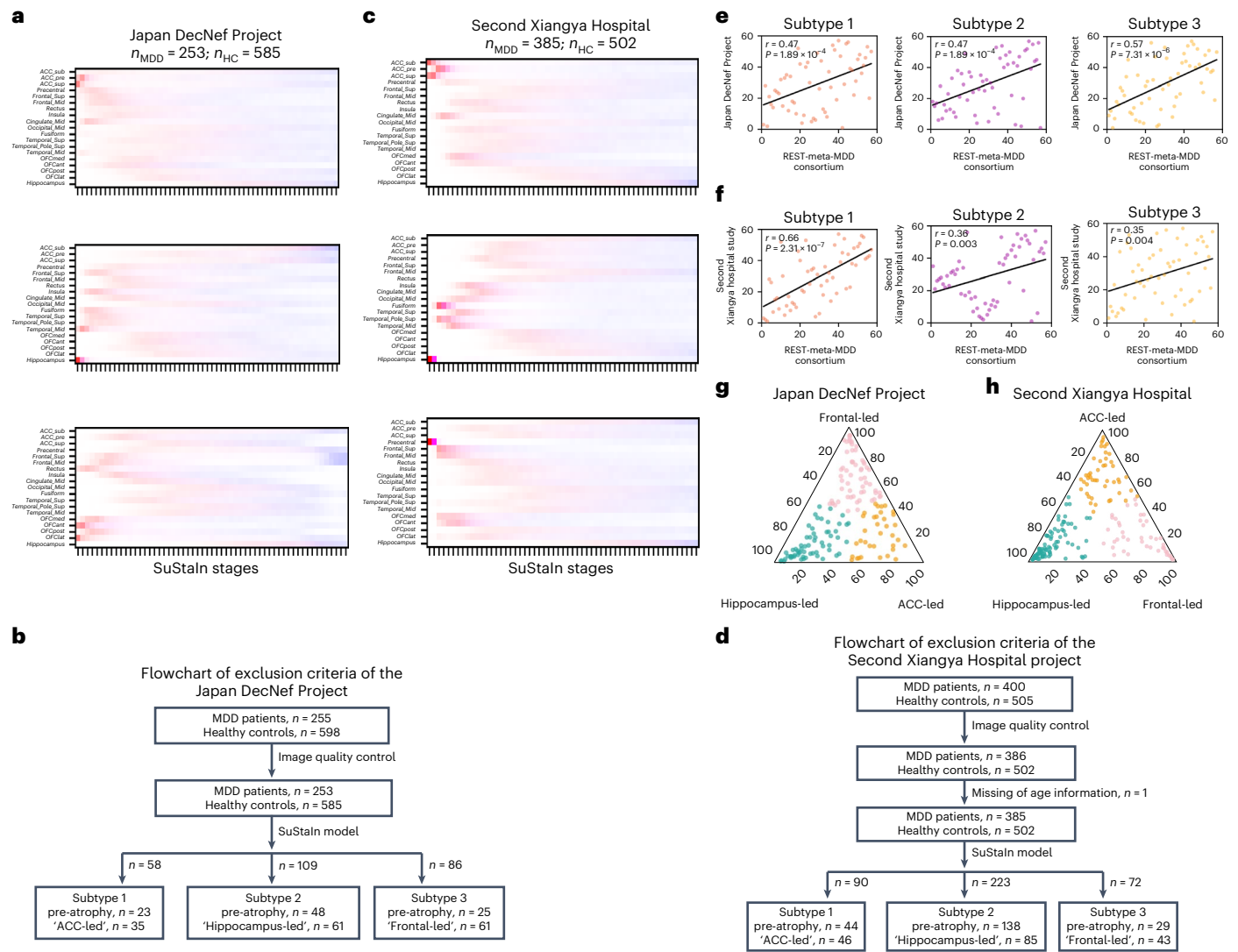


Fig. 3 | Robustness of MDD subtypes across two independent datasets. **a**, Three atrophy ‘trajectories’ in the Japan DecNef Project. **b**, Flowchart of exclusion criteria of the Japan DecNef Project. **c**, Three atrophy ‘trajectories’ in the Second Xiangya Hospital. **d**, Flowchart of exclusion criteria of the Second Xiangya Hospital. **e**, Order similarity of atrophy ‘trajectory’ between the discovery dataset and the Japan DecNef Project. Spearman’s rank correlation

test (one-tailed *P* value, FDR corrected) was used. **f**, Order similarity of atrophy ‘trajectory’ between the discovery dataset and the Second Xiangya Hospital. Spearman’s rank correlation test (one-tailed *P* value, FDR corrected) was used. **g**, The probability-based distribution of three MDD subtypes from the Japan DecNef Project. **h**, The probability-based distribution of three MDD subtypes from the Second Xiangya Hospital.

Robustness of MDD subtypes

We then applied the SuStaln procedure with identical parameters in two independent replication datasets from the Japan DecNef Project ($n_{MDD} = 253, n_{HC} = 585$; Fig. 3a,b and Supplementary Table 1) and the Second Xiangya Hospital ($n_{MDD} = 385, n_{HC} = 502$; Fig. 3c,d and Supplementary Table 1) and evaluated the similarity of atrophy ‘trajectories’ between the discovery and each replication dataset using the Spearman’s rank correlation between the corresponding sequences of progressive biomarkers (that is, $19 \times 3 = 57$). The observed SuStaln exportation (that is, order of atrophy ‘trajectory’) in both replication datasets showed significant consistency with the discovery dataset of the REST-meta-MDD project (Japan DecNef Project: $r = 0.47, P_{one-tailed} < 0.001$ for subtype 1; $r = 0.47, P_{one-tailed} < 0.001$ for subtype 2; $r = 0.57, P_{one-tailed} < 0.001$ for subtype 3; FDR corrected; Fig. 3e; Second Xiangya Hospital: $r = 0.66, P_{one-tailed} < 0.001$ for subtype 1; $r = 0.36, P_{one-tailed} = 0.003$ for subtype 2; $r = 0.35, P_{one-tailed} = 0.004$ for subtype 3; FDR corrected; Fig. 3f). The corresponding probability-based distributions of three post-atrophy

‘trajectories’ (that is, ‘ACC-led’, ‘hippocampus-led’ and ‘frontal-led’) of the Japan DecNef Project and Second Xiangya Hospital data are shown in Fig. 3g and Fig. 3h, respectively.

The consistent performance across three independent large sample MDD clinical neuroimaging datasets (that is, the REST-meta-MDD project, the Japan DecNef Project and the Second Xiangya Hospital project) confirmed the robustness of MDD subtypes.

Characterization of MDD subtypes by clinical profiles

We then asked how behavioural symptoms might link to the identified MDD anatomical subtypes. Multivariate analysis of variance (MANOVA)^{29,30} conducted to evaluate group differences among three MDD subtypes (that is, ‘ACC-led’, ‘hippocampus-led’ and ‘frontal-led’) across all 17 Hamilton depression rating scale (HAM-D) items found significant results ($\eta = 0.22$, adjusted $\eta = 0.11, P_{permu} = 0.0008$ based on 10,000 permutation iterations; Fig. 4a). With the significant MANOVA finding, we then conducted a one-way analysis of variance (ANOVA) to explore each HAM-D item’s group differences among MDD subtypes.

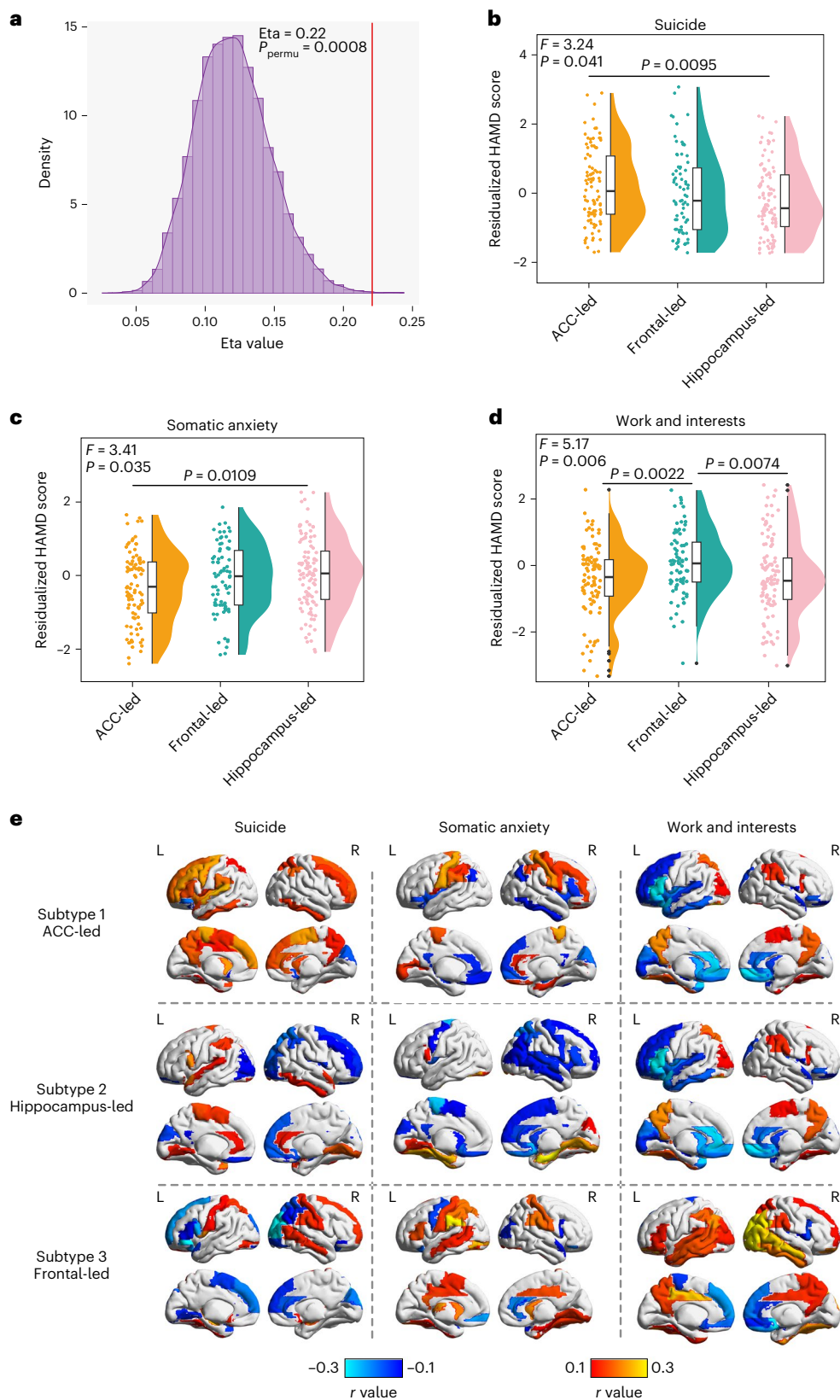


Fig. 4 | MDD subtypes are characterized by distinct clinical profiles. **a**, Eta values of 10,000 times permutation flow; one-tailed P value. **b–d**, Characteristic symptoms; ‘suicide’ risk score (**b**), ‘somatic anxiety’ behavioural score (**c**) and ‘work and interests’ score (**d**). $n_{\text{ACC-led}} = 93$, $n_{\text{hippocampus-led}} = 106$, $n_{\text{frontal-led}} = 77$; independent samples. One-way analysis of variance (ANOVA, one-tailed P value)

and post hoc t -test (two-tailed P value) were used. The data are presented through box plots (centre line: median; bounds of box: 25th percentile to 75th percentile; whiskers: maximum and minimum value of the data). **e**, Association between brain atrophy (z-scored GMV) and clinical profiles. L, left. R, right.

Notably, because these one-way ANOVA were essentially subsections of an already significant MANOVA, no further correction for multiple comparisons was needed³¹ (that is, the significant MANOVA effectively protected against inflated experiment-wise error rates of the following ANOVA). For clarity of presentation, the following terms were restricted to include only the HAMD items with a significant one-way ANOVA (that is, $P < 0.05$). Confounding factors including age, sex, years of education and site were first regressed out from the behavioural analyses.

The ‘ACC-led’ subtype displayed a high ‘suicide’ risk score (ANOVA: $F = 3.24$, $P = 0.041$; $t = 2.62$, Cohen's $d = 0.37$, $P_{\text{two-tailed}} = 0.0095$, $n_{\text{ACC-led}} = 93$, $n_{\text{hippocampus-led}} = 106$ for ‘ACC-led’ versus ‘hippocampus-led’; Fig. 4b and Supplementary Table 5). In contrast, the ‘hippocampus-led’ subtype exhibited high ‘somatic anxiety’ behavioural scores (ANOVA: $F = 3.41$, $P = 0.035$; $t = -2.57$, Cohen's $d = -0.37$, $P_{\text{two-tailed}} = 0.0109$, $n_{\text{ACC-led}} = 93$, $n_{\text{hippocampus-led}} = 106$ for ‘ACC-led’ versus ‘hippocampus-led’; Fig. 4c and Supplementary Table 5), whereas the ‘frontal-led’ showed impaired ‘work and interests’ score (ANOVA: $F = 5.17$, $P = 0.006$; $t = -3.10$, Cohen's $d = -0.48$, $P_{\text{two-tailed}} = 0.0022$, $n_{\text{ACC-led}} = 93$, $n_{\text{frontal-led}} = 77$, for ‘ACC-led’ versus ‘frontal-led’; $t = -2.71$, Cohen's $d = -0.41$, $P_{\text{two-tailed}} = 0.0074$, $n_{\text{hippocampus-led}} = 106$, $n_{\text{frontal-led}} = 77$ for ‘hippocampus-led’ versus ‘frontal-led’; Fig. 4d and Supplementary Table 5). In addition, the distinct relationships between brain atrophy of MDD subtypes and characteristic profiles were also observed (that is, higher z-scored GMV was positively associated with increasing symptoms; Fig. 4e), which again support behavioural differences among MDD subtypes.

Characterization of MDD subtypes by gene expression patterns

We first conducted a whole-brain voxel-based analysis of GMV contrasting three distinct ‘post-atrophy’ MDD subtypes to healthy controls. We then conducted the partial least square (PLS) analysis³² to ascertain the relationship between the voxel-based case–control differences (that is, the whole-brain t -map) of each subtype and the transcriptional activities of all 10,027 genes from AHBA. The derived first component of gene expression (PLS1) was the linear combination of gene expression that captured the greatest fraction of case–control GMV difference. As a result, the MDD brain pattern (that is, voxel-based case–control t -map) of the ‘ACC-led’ subtype demonstrated a significant correlation with its PLS1 ($r = 0.36$, $P_{\text{permu}} < 0.001$, Bonferroni corrected; Fig. 5a) after 1,000 iterations of standard permutation flow, as well as the ‘hippocampus-led’ subtype ($r = 0.42$, $P_{\text{permu}} < 0.001$, Bonferroni corrected; Fig. 5b), but not for the ‘frontal-led’ subtype ($r = 0.21$, $P_{\text{permu}} = 0.351$, Bonferroni corrected; Fig. 5c).

The gene-wise approach was then adopted to explore associations between the whole-brain t -maps of MDD subtypes and the transcriptional activity for each of the 10,027 genes. We first ranked the weights of PLS1 by one-sample z -tests. Using a stringent threshold ($z > 5$ for PLS1+ or $z < -5$ for PLS1-), we then identified 3,600 genes ($n = 1,883$ for PLS1+, $n = 1,717$ for PLS1-; all $P_{\text{FDR}} < 0.001$) for the ‘ACC-led’, 3,167 genes ($n = 1,874$ for PLS1+, $n = 1,293$ for PLS1-; all $P_{\text{FDR}} < 0.001$) for the ‘hippocampus-led’, and 1,480 genes ($n = 486$ for PLS1+, $n = 994$ for PLS1-; all $P_{\text{FDR}} < 0.001$) for the ‘frontal-led’. Finally, to characterize the biological functions of these identified genes, we conducted the enrichment analyses based on Gene Ontology (GO) and Kyoto Encyclopedia of Genes and Genomes (KEGG) using the R package ‘clusterProfiler’³³.

After FDR correction ($P_{\text{FDR}} < 0.05$), we identified two significant GO terms (Supplementary Table 6 and Supplementary Fig. 7) related to vessel formation enriched with ‘ACC-led’ PLS1+ genes (that is, ‘endothelium development’ and ‘endothelial cell differentiation’). Interestingly, the endothelial progenitor cells that underlie blood vessel regeneration have long been associated with depressive symptoms, although the underlying mechanism remains unclear^{34–36}. In addition, 66 GO terms (for example, ‘vesicle-mediated transport in synapse’; Supplementary Table 7 and Supplementary Fig. 7) and 13 KEGG pathways, such as

‘neuroactive ligand–receptor interaction’, were enriched with ‘ACC-led’ PLS1– genes (Supplementary Table 8 and Supplementary Fig. 7).

Further, we identified 31 GO terms (for example, ‘RNA processing’; Supplementary Table 9 and Supplementary Fig. 8) and 2 KEGG pathways (for example, ‘ribosome’; Supplementary Table 10 and Supplementary Fig. 8) for the ‘hippocampus-led’ PLS1+ genes, as well as 123 GO terms (for example, ‘axon development’ and ‘neuron projection morphogenesis’; Supplementary Table 11 and Supplementary Fig. 8) and 4 KEGG pathways (for example, ‘axon guidance’ and ‘neuroactive ligand–receptor interaction’) for ‘hippocampus-led’ PLS1– genes (Supplementary Table 12 and Supplementary Fig. 8).

Finally, we identified 11 GO terms (for example, ‘regulation of tissue remodelling’; Supplementary Table 13 and Supplementary Fig. 9) and 3 KEGG pathways (that is, ‘notch signalling pathway’; Supplementary Table 14 and Supplementary Fig. 9) enriched with ‘frontal-led’ PLS1+ genes, and 26 GO terms (for example, ‘distal axon’; Supplementary Table 15 and Supplementary Fig. 9) and 2 KEGG pathways (for example, ‘neuroactive ligand–receptor interaction’; Supplementary Table 16 and Supplementary Fig. 9) enriched with ‘frontal-led’ PLS1– genes.

Differentiated MDD gene expression patterns of MDD subtypes

The first and second principal component analysis (that is, PCA1 and PCA2) scores of 12 MDD-related genes (‘ADRA2A’, ‘CHRM2’, ‘CNRI’, ‘CRH’, ‘CUX2’, ‘GAD2’, ‘HTRIA’, ‘HTR5A’, ‘MAOA’, ‘PDE1A’, ‘SST’ and ‘TAC1’; Supplementary Table 17; for more details, see Methods) were estimated to preserve the maximum amount of genetic information. We observed significant correlations between the PCA1 with the ‘ACC-led’ ($r = 0.16$, $P_{\text{permu}} = 0.032$, FDR corrected; Fig. 5d) and ‘hippocampus-led’ brain pattern ($r = 0.21$, $P_{\text{permu}} = 0.004$, FDR corrected; Fig. 5e), but not with the ‘frontal-led’ pattern ($r = -0.02$, $P_{\text{permu}} = 0.836$, FDR corrected; Fig. 5f). Unlike PCA1, PCA2 demonstrated significant associations with both brain patterns of the ‘ACC-led’ ($r = -0.29$, $P_{\text{permu}} < 0.001$, FDR corrected; Fig. 5d) and the ‘frontal-led’ ($r = -0.19$, $P_{\text{permu}} = 0.006$, FDR corrected; Fig. 5f), but not with the ‘hippocampus-led’ ($r = -0.07$, $P_{\text{permu}} = 0.406$, FDR corrected; Fig. 5e).

We further evaluated the relationships between MDD-related genes and distinct brain patterns of MDD subtypes. After 1,000 iterations of standard permutation flow and with FDR correction, we identified five MDD-related genes (that is, ‘CNRI’, ‘GAD2’, ‘HTRIA’, ‘MAOA’ and ‘SST’; Fig. 5g and Supplementary Table 18) that were significantly relevant ($P_{\text{permu}} < 0.001$, FDR corrected) to the brain pattern for ‘hippocampus-led’ subtype, one gene for ‘frontal-led’ subtype (that is, ‘SST’; Fig. 5g and Supplementary Table 18) and five genes for ‘ACC-led’ subtype (that is, ‘CNRI’, ‘HTRIA’, ‘PDE1A’, ‘SST’ and ‘TAC1’; Fig. 5g and Supplementary Table 18). Notably, the ‘hippocampus-led’ patients with MDD showed specificity for ‘GAD2’ and ‘MAOA’ genes ($r = 0.20$, $P_{\text{permu}} < 0.001$ for ‘GAD2’; $r = -0.23$, $P_{\text{permu}} < 0.001$ for ‘MAOA’; FDR corrected) whereas ‘ACC-led’ individuals showed specificity for ‘PDE1A’ and ‘TAC1’ genes ($r = -0.26$, $P_{\text{permu}} < 0.001$ for ‘PDE1A’; $r = -0.13$, $P_{\text{permu}} = 0.029$ for ‘TAC1’; FDR corrected) (for details, see Fig. 5g and Supplementary Table 18).

Discussion

The progression of neural atrophy in MDD has been previously reported, but little is known about the underlying neurobiological mechanisms, particularly their distinct progressive patterns or ‘trajectories’. Here, using the data-driven SuStain algorithm on a large clinical sample with neuroimaging, we highlighted three different ‘trajectories’ of spatiotemporal atrophy: the first ‘trajectory’ began with subgenual anterior cingulate cortex (sgACC) atrophy that progressively encompassed the whole ACC; the second ‘trajectory’ showed initial hippocampal atrophy and progressively affected temporal substrates; and the third ‘trajectory’ initiated with SFG atrophy and progressed into the middle frontal and orbitofrontal cortices. These different anatomical ‘trajectories’ were also linked to distinct behavioural symptoms: suicide

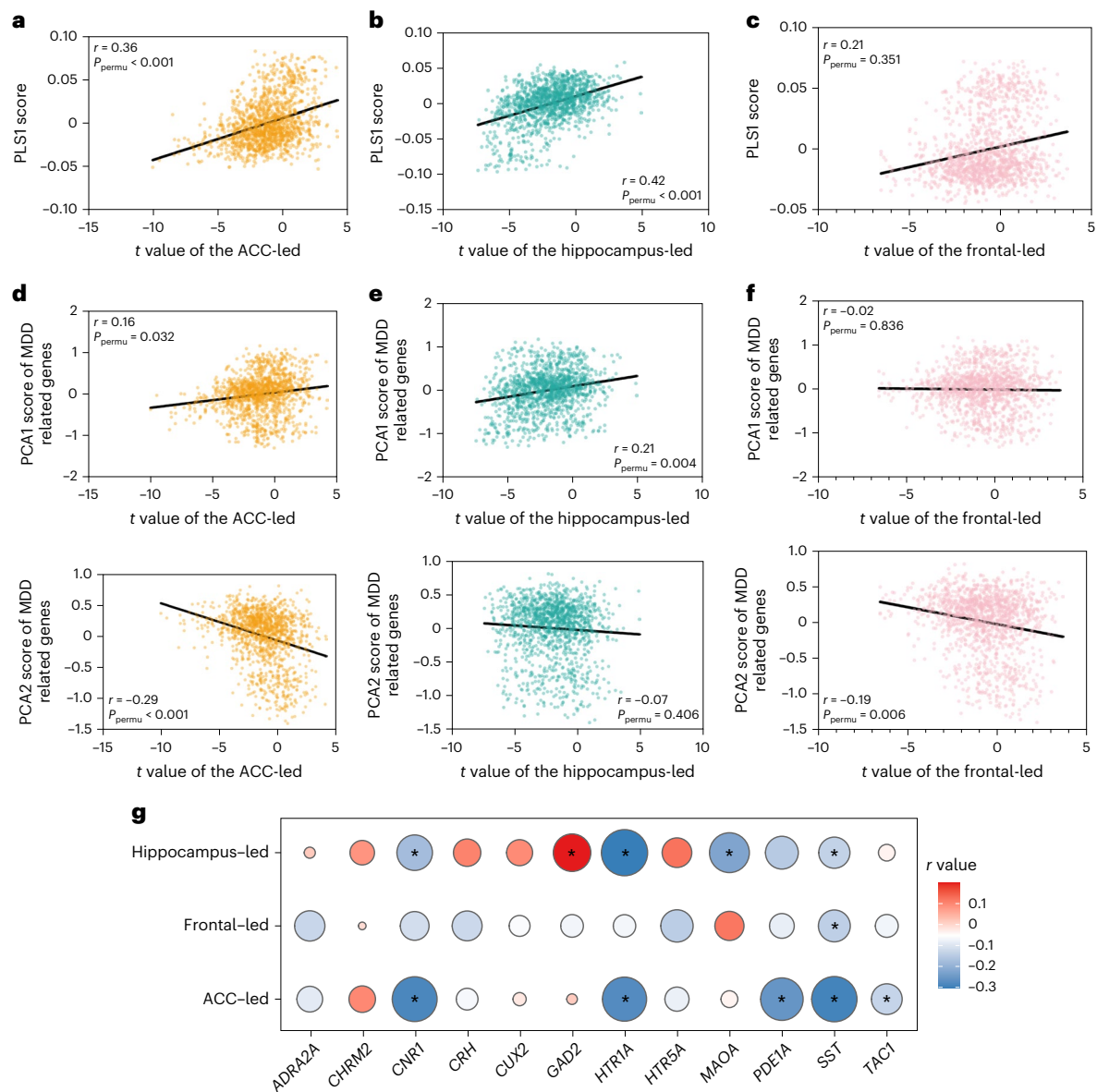


Fig. 5 | Distinct 'gene expression-brain' profiles of MDD subtypes. **a–c.** The first component of PLS (that is, PLS1) was employed to evaluate the relationship between the voxel-based case-control differences (that is, the whole-brain t -map) of each subtype (ACC-led (**a**), hippocampus-led (**b**) and frontal-led (**c**)) and the transcriptional activities of all 10,027 genes from AHBA; Pearson correlation test (one-tailed P value, Bonferroni corrected) was used. **d–f.** Associations

between the first two principal components of 12 MDD-related genes and the whole-brain t -map of each MDD subtype (ACC-led (**d**), hippocampus-led (**e**) and frontal-led (**f**)); two-tailed P value, FDR corrected. **g.** MDD-related genes were differentially expressed in different MDD subtypes. The r values and P values can be found in Supplementary Table 18; all P values were evaluated with 1,000 times permutation; FDR-corrected two-tailed $*P < 0.05$.

risk was highest in patients from the 'ACC-led' subtype; somatic anxiety was primarily observed in the 'hippocampus-led' subtype; and loss of interest in daily life was most severe in the 'frontal-led' subtype. As further evidence to support the biological plausibility of the three distinct subtypes, we demonstrated specific gene expression patterns for each 'trajectory'. Remarkably, the MDD-related genes were dissociable between the three different 'trajectories'. Further, the robustness of the three atrophy subtypes was supported, not only by the moderate to large sample size in the discovery dataset, but also by validation in two independent datasets, hence illustrating the high reproducibility of the 'trajectories'. Thus, we highlight the clinical implications of these three subtypes identified by spatiotemporal atrophy differentiation, behavioural markers and genetic differences in patients with MDD, which may be relevant for potential individualized diagnoses and predictions of clinical trajectories.

The 'ACC-led' subtype suggests the sgACC as a pathophysiological origin of MDD (Fig. 2b), which is in line with previous studies^{13,37–39}. The sgACC shows extensive interactions with key features of MDD implicated across mood, somatic and cognitive symptoms and plays a critical role in regulating mood states, sustaining autonomic arousal and worsening negative MDD symptoms (for example, rumination)^{21,40}. This ACC-origin theory is further supported by findings that young individuals with MDD show significantly reduced ACC γ -aminobutyric acid⁴¹. Finally, sgACC activity could be improved in MDD following multiple forms of successful therapeutic interventions, including psychotherapy, antidepressants and ketamine infusion⁴², and the sgACC is also the target for deep brain stimulation for MDD⁴³ and its hypoconnectivity with dorsolateral prefrontal cortex is an effective biomarker to optimize repetitive transcranial magnetic stimulation targeting⁴⁴. Together these findings highlighted

a potentially stratified treatment strategy targeting the ‘ACC-led’ subtype in therapeutic interventions.

The hippocampus is implicated as a brain region for emotional responses, learning and memory⁴⁵ and converting short-term memory into long-term memory. Using the SuStaIn algorithm, we identified this brain area as the pathophysiological origin of the ‘hippocampus-led’ subtype, which is consistent with reductions of hippocampal volume observed in patients with early-onset MDD from previous studies^{14,46}. In longitudinal studies, the hippocampal volume has also been reported to progressively decrease during the MDD disease course beyond that of normal ageing⁴⁷, thus supporting hippocampal changes observed with SuStaIn stages.

The OFC plays a core role in emotion, pleasure and decision-making, representing the primary reinforcers’ reward value⁴⁸. Patients with MDD show lower volumes of the SFG and OFC, in line with other structural MRI studies^{2,13}. As a genetic verification from the UK Biobank study, the polygenic risk score of anhedonia has also shown an association with OFC volumes^{2,49}. For the ‘frontal-led’ subtype of patients with MDD, we demonstrated the SFG and OFC as the neural origin. OFC abnormalities in patients with MDD have been reported to emerge early and have a negative effect on emotion regulation^{2,50}, supporting the frontal-led theory. Resting-state functional connectivity in patients with MDD shows abnormalities within networks anchored on different OFC regions⁵. Furthermore, targeting the dorsomedial prefrontal cortex⁵¹ (adjacent to the SFG) and OFC⁵² with repetitive transcranial magnetic stimulation has shown evidence for efficacy in MDD therapy. In summary, the identified MDD subtypes might be responsive to alternative targeting strategies.

The above argument was further supported by the findings that different MDD subtypes demonstrate distinct behavioural symptoms. Suicide risk was found highest for the ‘ACC-led’ subtype, moderate for the ‘hippocampus-led’ and lowest for the ‘frontal-led’ subtype (Fig. 4b), which converges well with previous studies^{2,53}. Also, a decrease in dorsal ACC-pregenual ACC resting-state functional connectivity has been shown to correlate with a reduction in suicidal risk⁵³. Further, the ‘frontal-led’ subtype displayed significantly higher impairment in ‘work and interests’ score than the other subtypes, indicating lower motivation for this subtype, which is in line with OFC’s implicated role in reward-guided learning and decision-making⁵⁴. Finally, we showed a dedicated relationship between somatic anxiety and the ‘hippocampal-led’ subtype. As MDD has also been reported as a risk factor for the development of Alzheimer’s disease⁵⁵, further longitudinal studies investigating the clinical implications for this subtype in tracking memory deficits or as a prodromal state are needed. Furthermore, MDD-related genes also displayed differing transcriptional correlates of the three subtypes (Fig. 5g), indicating distinct origins and confirming biological plausibility for differentiating these ‘trajectories’. These findings demonstrated that characteristic symptoms linked to these ‘trajectories’ may contribute to individualized diagnoses, highlighting the risk for suicide and optimal therapeutic targeting.

Finally, the identified MDD subtypes are highly robust, as they have been successfully replicated in two independent cohorts (Fig. 3a,c), and they also demonstrate highly similar trajectories in the presence or absence of medical treatment (Supplementary Fig. 4). However, while we acknowledge that different classes of medication may have different impacts on the progression of MDD subtypes, our current datasets do not have relevant information. Therefore, future research focusing on different medications would be useful to further our understanding of brain atrophy in MDD.

In conclusion, we identified three highly robust ‘trajectories’ of brain atrophy in patients with MDD starting in the sgACC, hippocampus and SFG/OFC, respectively, and each ‘trajectory’ demonstrates distinct clinical profiles and transcriptomic correlates. Our data-driven findings demonstrate the existence of subtypes in MDD and may contribute to the future stratified medicine and intervention.

Methods

Participants

A total of 1,151 patients with MDD and 1,064 HC individuals from the REST-meta-MDD project^{10,26} (age 37.21 ± 14.64 years, 68% female for MDD; age 36.35 ± 15.53 years, 60% female for HC) were included as the discovery dataset. For two replication datasets, the strategic research programme for brain sciences of the DecNef Project from Japan ($n_{\text{MDD}} = 253$, $n_{\text{HC}} = 585$, age 42.49 ± 11.99 , 47% female for MDD; age 39.69 ± 15.48 years, 55% female for HC²⁷) and the Second Xiangya Hospital study ($n_{\text{MDD}} = 385$, $n_{\text{HC}} = 502$, age 23.20 ± 6.42 years, 68% female for MDD; age 21.45 ± 3.91 years, 64% female for HC) were also investigated. Based on the geographical location of the local hospitals, the participants’ ethnicity was identified (Chinese for the REST-meta-MDD project, Japanese for the Japan DecNef Project and Chinese for the Second Xiangya Hospital study). MDD patient diagnosis was confirmed by the structured clinical interview with the International Statistical Classification of Diseases and Related Health Problems 10th Revision or the Diagnostic and Statistical Manual of Mental Disorders, 4th Edition. The self-reported ‘sex’ was used due to its biological attribution. All participants agreed to provide clinical diagnosis, age, sex and years of education. The demographic characteristics are summarized in Supplementary Table 1.

Ethical permission was approved by the medical research ethics committee (no. H19045 for the REST-meta-MDD project; Advanced Telecommunications Research Institute International (nos. 13–133, 14–133, 15–133, 16–133, 17–133 and 18–133), Hiroshima University (nos. E-172, E-38), Kyoto Prefectural University of Medicine (no. RBMR-C-1098), Showa University (nos. B-2014-019 and UMIN000016134), the University of Tokyo Faculty of Medicine (no. 3150), Kyoto University (nos. C809 and R0027), Osaka University (no. 13384), and CiNet (no. 20140611) for the Japan DecNef Project; and no. 2019-075 for the Second Xiangya Hospital study) and signed informed consent was obtained from all participants. The trial registration number for this study is ChiCTR2000031931 (ref. 56).

Image pre-processing and quality control

Structural T1-weighted MRI brain scans were collected for each dataset. Using the voxel based morphometry (VBM) 8 toolbox⁵⁷, the office of the REST-meta-MDD project conducted standard pre-processing as reported in previous studies^{10,58}. Aligned with the REST-meta-MDD project, similar image pre-processing was conducted for the Japan DecNef Project and the Second Xiangya Hospital study, and briefly described as follows: we first segmented the structural T1-weighted MRI into grey matter, white matter and CSF using a unified segmentation routine⁵⁹. We then employed the diffeomorphic anatomical registration through exponential lie algebra tool⁶⁰ to transform individual native space into standard Montreal Neurological Institute space with $1.5 \times 1.5 \times 1.5 \text{ mm}^3$ resolution with an iterative registration. We modulated the grey matter maps to correct for volumetric distortions (based on the Jacobian of the spatially normalizing deformations), resulting in grey matter images.

We used the 2nd edition AAL-2 (ref. 61) template to parcellate the brain into 120 ROIs and the 3rd edition AAL-3 (ref. 62) to split the ACC into three ROIs (that is, subgenual ACC, pregenual ACC and supracallosal ACC). We further extracted each ROI by averaging the signals of all voxels included.

Using the R package flashClust, imaging outliers were identified if showing negative correlations with most of the rest of the individuals in terms of the whole-brain similarity and hence removed; for details, see Supplementary Figs. 10–12.

Feature selection

Due to the heavy computing resource demanding of the SuStaIn model²³, we restricted the number of input ROIs below 20 ($n < 20$), which contains brain cortical regions with the largest atrophy (that is,

MDD versus HC: $P_{\text{FDR}} < 0.001$ for each selected region, FDR corrected) in the REST-meta-MDD data, plus additional candidate ROIs (hippocampus and OFCs) following findings from the Enhancing Neuroimaging Genetics through Meta-Analysis consortium^{11,13}. As a result, 19 ROIs (Fig. 2b) were finally entered into the SuStaln model to yield 57 sequenced events (that is, 19 ROIs multiplied by three severity thresholds, $z = [1, 1.5, 2]$, gives a total of 57 stages). In the present study, we calculated the mean value of two ROIs from the left and right hemispheres.

The SuStaln model

Previous investigations have explored the use of imaging biomarkers to identify subtype of MDD^{7,22}, yet the relatively low replicability prevents us from using these characteristics. As a novel algorithm, the SuStaln model allows us to evaluate the neural atrophy subtype of MDD, which has exhibited excellent performance in identifying the distinct ‘trajectories’ of Alzheimer’s disease²⁴.

Confounding factors such as the TIV, age, sex, years of education and site were first regressed out from ROIs for the REST-meta-MDD project. The adjusted ROI that fed into the SuStaln model was z -scored relative to the population of the HCs and was calculated as: $Y_{\text{zscore}} = (-1) \times \frac{Y_i - \text{mean}(X)}{\text{std}(X)}$, where X denotes GMVs of HC individuals and Y_i is the GMV of the i th patient with MDD. As a result, the higher z -value represents severe brain atrophy condition relative to HCs. Three z -scores (1, 1.5 and 2) were employed as cut-offs of MDD severity to describe the disease progression for the model.

For two replication datasets (that is, Japan DecNef Project and Second Xiangya Hospital study), the TIV, age, sex and site were also regressed out from ROIs first. The adjusted ROIs were then fed into SuStaln model with identical parameters and aligned with the discovery dataset. Post hoc power analyses were conducted for the primary results of this study using G*Power⁶³; for details, see Supplementary Table 19.

The optimal number of MDD subtypes

To identify the number of subtypes, as there is no consistent conclusion from previous studies⁶⁴, we used the CVIC and out-of-sample log-likelihood²³ to evaluate the performance. We employed a five-fold cross-validation of the SuStaln data to determine the optimal number of subtypes, which was calculated with different cluster numbers from 1 to 5. Lower CVIC and higher log-likelihood represent better performance in the SuStaln algorithm²³. The three-cluster partition was the optimal choice, which showed the minimum CVIC (Supplementary Fig. 3a) and maximal log-likelihood (Supplementary Fig. 3b). Hence the optimal three-cluster separation indicated that there are three distinct GMV-based atrophy progressions in patients with MDD.

Three distinct gene expressions of atrophy patterns

The AHBA dataset (<http://human.brain-map.org>)⁶⁵ was employed to investigate the gene expression of MDD subtypes, which is a well-known brain transcriptomic dataset^{66,67}. Only the left hemisphere from six samples was used in the present study. Following a previous paper by Arnatkeviciute et al.²⁸, we implemented standard pre-processing of the AHBA dataset, including (1) the Re-annotator toolkit to identify the probe-to-gene annotations. (2) Intensity-based filtering and probe selection were performed. For each sample in the AHBA dataset, every probe has been assigned a binary indicator (that is, intensity-based filtering) to determine if it measures an expression signal surpassing the background levels²⁸. To discriminate expression signal from noise, we used the intensity-based filtering²⁸, which is based on a t -test criterion as outlined in the AHBA documentation⁶⁸. After intensity-based filtering (that is, excluding probes that do not exceed the background noise threshold) and probe selection (that is, selecting microarray probes that have the highest correlation with the corresponding RNA-seq data), 10,027 genes were finally used in the present study^{28,66}. (3) Samples were assigned within 2-mm Euclidean

distance of a parcel. For the sample brain region distance, we computed the distance by taking the minimum distance between the sample and any voxel in the region^{69–71}, not by its centroid coordinate. This approach has been shown to be highly accurate for regions in any given parcellations irrespective of the size and folded geometry²⁸. (4) We also conducted the scaled robust sigmoid normalization⁷² to control for heterogeneity due to donor difference. This approach normalizes gene expression based on the outlier-robust sigmoid function, which ensures equivalent scaling of expression values for each person in AHBA²⁸.

The whole-brain analysis of GMV contrasting MDD and HC was then conducted to identify three MDD patterns (that is, whole-brain t -map). Finally, the statistical t -map was aligned to the transcriptomic data by the voxel-based coordinate of the MNI152 standard space. After standard pre-processing and intersection with the voxel-based brain template, we acquired a transcriptional matrix (1,397 locus \times 10,027 gene expression).

The selection of MDD-related genes

We investigated if previously reported MDD genes could also distinguish different atrophy-based subtypes. We chose previously defined MDD-related genes⁶⁶ from the ‘Genes characterized by ISH in 1000 gene survey in cortex’ dataset provided by the AHBA⁶⁸. The 12 MDD-related genes (that is, ‘ADRA2A’, ‘CHRM2’, ‘CNRI’, ‘CRH’, ‘CUX2’, ‘GAD2’, ‘HTR1A’, ‘HTR5A’, ‘MAOA’, ‘PDE1A’, ‘SST’ and ‘TAC1’; for details, see Supplementary Table 17) were included after the search with ‘depression’ in the ‘Gene List’ and intersection with 10,027 total genes from the AHBA.

Reporting summary

Further information on research design is available in the Nature Portfolio Reporting Summary linked to this article.

Data availability

The data of the AHBA microarray dataset are available from the website <http://human.brain-map.org>. The data of REST-meta-MDD project from the DIRECT Consortium are available from the website <http://www.rfmri.org/REST-meta-MDD>. The data from the Japan DecNef Project are available from the website <https://bicy.atr.jp/decnefpro/>. The data from Second Xiangya Hospital within the ZIB Consortium are not available for public download, but access can be requested through the corresponding author J.F. (jffeng@fudan.edu.cn). Requests for raw and analysed data will be promptly reviewed by the Fudan University ethics committee to verify whether the request is subject to any intellectual property or confidentiality obligations.

Code availability

Python (version: 3.9.6) was employed to perform the SuStaln algorithm (<https://github.com/ucl-pond>). BrainNet Viewer (version: 20191031) was used to visualize ROI-wise images. MATLAB (version: 2018b) was employed to perform the other analyses, including correlation analysis and t -test. R package flashClust (version 1.01–2) was used to imaging quality control. R package clusterProfiler (version 4.8.2) was employed for enrichment analysis. VBM (version VBM 8) was used to process the imaging data. G*Power (version 3.1) was employed for the power analyses. The primary codes developed in the current study are available at GitHub (<https://github.com/dichen27/>).

References

1. Malhi, G. S. & Mann, J. J. Depression. *Lancet* **392**, 2299–2312 (2018).
2. Pizzagalli, D. A. & Roberts, A. C. Prefrontal cortex and depression. *Neuropsychopharmacology* **47**, 225–246 (2022).
3. Schmaal, L. et al. ENIGMA MDD: seven years of global neuroimaging studies of major depression through worldwide data sharing. *Transl. Psychiatry* **10**, 172 (2020).

4. Musil, R. et al. Subtypes of depression and their overlap in a naturalistic inpatient sample of major depressive disorder. *Int. J. Methods Psychiatr. Res.* **27**, e1569 (2018).
5. Cheng, W. et al. Medial reward and lateral non-reward orbitofrontal cortex circuits change in opposite directions in depression. *Brain* **139**, 3296–3309 (2016).
6. Saveanu, R. V. & Nemeroff, C. B. Etiology of depression: genetic and environmental factors. *Psychiatr. Clin. North Am.* **35**, 51–71 (2012).
7. Drysdale, A. T. et al. Resting-state connectivity biomarkers define neurophysiological subtypes of depression. *Nat. Med.* **23**, 28–38 (2017).
8. Nestler, E. J. & Hyman, S. E. Animal models of neuropsychiatric disorders. *Nat. Neurosci.* **13**, 1161–1169 (2010).
9. Chen, D. et al. Brain signatures during reward anticipation predict persistent attention-deficit/hyperactivity disorder symptoms. *J. Am. Acad. Child. Psychiatry* **61**, 1050–1061 (2022).
10. Yan, C.-G. et al. Reduced default mode network functional connectivity in patients with recurrent major depressive disorder. *Proc. Natl Acad. Sci. USA* **116**, 9078–9083 (2019).
11. Schmaal, L. et al. Subcortical brain alterations in major depressive disorder: findings from the ENIGMA Major Depressive Disorder working group. *Mol. Psychiatry* **21**, 806–812 (2016).
12. Tao, H. et al. Depression uncouples brain hate circuit. *Mol. Psychiatry* **18**, 101–111 (2013).
13. Schmaal, L. et al. Cortical abnormalities in adults and adolescents with major depression based on brain scans from 20 cohorts worldwide in the ENIGMA Major Depressive Disorder Working Group. *Mol. Psychiatry* **22**, 900–909 (2017).
14. Renteria, M. E. et al. Subcortical brain structure and suicidal behaviour in major depressive disorder: a meta-analysis from the ENIGMA-MDD working group. *Transl. Psychiatry* **7**, e1116 (2017).
15. Tozzi, L. et al. Interactive impact of childhood maltreatment, depression, and age on cortical brain structure: mega-analytic findings from a large multi-site cohort. *Psychol. Med.* **50**, 1020–1031 (2020).
16. de Kovel, C. G. F. et al. No alterations of brain structural asymmetry in major depressive disorder: an ENIGMA consortium analysis. *Am. J. Psychiatry* **176**, 1039–1049 (2019).
17. Tolomeo, S. et al. A causal role for the anterior mid-cingulate cortex in negative affect and cognitive control. *Brain* **139**, 1844–1854 (2016).
18. He, Z. L. et al. Functional dysconnectivity within the emotion-regulating system is associated with affective symptoms in major depressive disorder: a resting-state fMRI study. *Aust. NZ J. Psychiatry* **53**, 528–539 (2019).
19. Fitzgerald, P. B., Laird, A. R., Maller, J. & Daskalakis, Z. J. A meta-analytic study of changes in brain activation in depression. *Hum. Brain Mapp.* **29**, 683–695 (2008).
20. Grimm, S. et al. Imbalance between left and right dorsolateral prefrontal cortex in major depression is linked to negative emotional judgment: an fMRI study in severe major depressive disorder. *Biol. Psychiatry* **63**, 369–376 (2008).
21. Cooney, R. E., Joormann, J., Eugene, F., Dennis, E. L. & Gotlib, I. H. Neural correlates of rumination in depression. *Cogn. Affect. Behav. Neurosci.* **10**, 470–478 (2010).
22. Shah, P. J., Glabus, M. F., Goodwin, G. M. & Ebmeier, K. P. Chronic, treatment-resistant depression and right fronto-striatal atrophy. *Br. J. Psychiatry* **180**, 434–440 (2002).
23. Young, A. L. et al. Uncovering the heterogeneity and temporal complexity of neurodegenerative diseases with subtype and stage inference. *Nat. Commun.* **9**, 4273 (2018).
24. Vogel, J. W. et al. Four distinct trajectories of tau deposition identified in Alzheimer’s disease. *Nat. Med.* **27**, 871–881 (2021).
25. Jiang, Y. et al. Neuroimaging biomarkers define neurophysiological subtypes with distinct trajectories in schizophrenia. *Nat. Ment. Health* **1**, 186–199 (2023).
26. Chen, X. et al. The DIRECT consortium and the REST-meta-MDD project: towards neuroimaging biomarkers of major depressive disorder. *Psychoradiology* **2**, 32–42 (2022).
27. DecNef Project. Japan Agency for Medical Research and Development <https://bicr.atr.jp/decnefpro/> (2017).
28. Arnatkeviciute, A., Fulcher, B. D. & Fornito, A. A practical guide to linking brain-wide gene expression and neuroimaging data. *NeuroImage* **189**, 353–367 (2019).
29. Stevens, J. *Applied Multivariate Statistics for the Social Sciences* (Lawrence Erlbaum Associates, 2002).
30. Jia, T. Y. et al. Neurobehavioural characterisation and stratification of reinforcement-related behaviour. *Nat. Hum. Behav.* **4**, 544–558 (2020).
31. Bernhardson, C. S. Type-I error rates when multiple comparison procedures follow a significant *F* test of ANOVA. *Biometrics* **31**, 229–232 (1975).
32. Abdi, H. Partial least squares regression and projection on latent structure regression (PLS regression). *Wiley Interdiscip. Rev. Comput. Stat.* **2**, 97–106 (2010).
33. Yu, G. C., Wang, L.-G., Han, Y. Y. & He, Q.-Y. clusterProfiler: an R package for comparing biological themes among gene clusters. *Omic* **16**, 284–287 (2012).
34. Dome, P. et al. Circulating endothelial progenitor cells and depression: a possible novel link between heart and soul. *Mol. Psychiatry* **14**, 523–531 (2009).
35. Di Stefano, R. et al. Impact of depression on circulating endothelial progenitor cells in patients with acute coronary syndromes: a pilot study. *J. Cardiovasc. Med.* **15**, 353–359 (2014).
36. Fiedorowicz, J. G., Ellingrod, V. L., Kaplan, M. J. & Sen, S. The development of depressive symptoms during medical internship stress predicts worsening vascular function. *J. Psychosom. Res.* **79**, 243–245 (2015).
37. Hamani, C. et al. The subcallosal cingulate gyrus in the context of major depression. *Biol. Psychiatry* **69**, 301–308 (2011).
38. Barthas, F. et al. The anterior cingulate cortex is a critical hub for pain-induced depression. *Biol. Psychiatry* **77**, 236–245 (2015).
39. Cooney, R. E., Joormann, J., Atlas, L. Y., Eugene, F. & Gotlib, I. H. Remembering the good times: neural correlates of affect regulation. *NeuroReport* **18**, 1771–1774 (2007).
40. Rudebeck, P. H. et al. A role for primate subgenual cingulate cortex in sustaining autonomic arousal. *Proc. Natl Acad. Sci. USA* **111**, 5391–5396 (2014).
41. Gabbay, V. et al. Anterior cingulate cortex gamma-aminobutyric acid deficits in youth with depression. *Transl. Psychiatry* **7**, e1216 (2017).
42. Morris, L. S. et al. Ketamine normalizes subgenual cingulate cortex hyper-activity in depression. *Neuropsychopharmacology* **45**, 975–981 (2020).
43. Johansen-Berg, H. et al. Anatomical connectivity of the subgenual cingulate region targeted with deep brain stimulation for treatment-resistant depression. *Cereb. Cortex* **18**, 1374–1383 (2008).
44. Liston, C. et al. Default mode network mechanisms of transcranial magnetic stimulation in depression. *Biol. Psychiatry* **76**, 517–526 (2014).
45. Frodl, T. et al. Reduced hippocampal volume correlates with executive dysfunctioning in major depression. *J. Psychiatry Neurosci.* **31**, 316–323 (2006).
46. Caetano, S. C. et al. Medial temporal lobe abnormalities in pediatric unipolar depression. *Neurosci. Lett.* **427**, 142–147 (2007).
47. Frodl, T. S. et al. Depression-related variation in brain morphology over 3 years—effects of stress? *Arch. Gen. Psychiatry* **65**, 1156–1165 (2008).

48. Rolls, E. T. The orbitofrontal cortex and emotion in health and disease, including depression. *Neuropsychologia* **128**, 14–43 (2019).
49. Ward, J. et al. Novel genome-wide associations for anhedonia, genetic correlation with psychiatric disorders, and polygenic association with brain structure. *Transl. Psychiatry* **9**, 327 (2019).
50. Hiser, J. & Koenigs, M. The multifaceted role of the ventromedial prefrontal cortex in emotion, decision making, social cognition, and psychopathology. *Biol. Psychiatry* **83**, 638–647 (2018).
51. Dunlop, K. et al. Dorsomedial prefrontal cortex repetitive transcranial magnetic stimulation for treatment-refractory major depressive disorder: a three-arm, blinded, randomized controlled trial. *Brain Stimul.* **13**, 337–340 (2020).
52. Feffer, K. et al. 1 Hz rTMS of the right orbitofrontal cortex for major depression: safety, tolerability and clinical outcomes. *Eur. Neuropsychopharmacol.* **28**, 109–117 (2018).
53. Chen, M.-H. et al. Antidepressant and antisuicidal effects of ketamine on the functional connectivity of prefrontal cortex-related circuits in treatment-resistant depression: a double-blind, placebo-controlled, randomized, longitudinal resting fMRI study. *J. Affect. Disord.* **259**, 15–20 (2019).
54. Zhou, J. F., Gardner, M. P. H. & Schoenbaum, G. Is the core function of orbitofrontal cortex to signal values or make predictions? *Curr. Opin. Behav. Sci.* **41**, 1–9 (2021).
55. Santos, L. E., Beckman, D. & Ferreira, S. T. Microglial dysfunction connects depression and Alzheimer's disease. *Brain Behav. Immun.* **55**, 151–165 (2016).
56. Zhangjing International Brain Biobank Depression Cohort Data Collection and Data Mining. *Chinese Clinical Trial Registry* <https://www.chictr.org.cn/showproj.html?proj=51913> (2020).
57. The VBM 8 toolbox (University College London, 2009); <https://www.fil.ion.ucl.ac.uk/spm/software/spm8/>
58. Yan, C.-G., Wang, X.-D., Zuo, X.-N. & Zang, Y.-F. DPABI: data processing & analysis for (resting-state) brain imaging. *Neuroinformatics* **14**, 339–351 (2016).
59. Ashburner, J. & Friston, K.J. Unified segmentation. *NeuroImage* **26**, 839–851 (2005).
60. Ashburner, J. A fast diffeomorphic image registration algorithm. *NeuroImage* **38**, 95–113 (2007).
61. Rolls, E. T., Joliot, M. & Tzourio-Mazoyer, N. Implementation of a new parcellation of the orbitofrontal cortex in the automated anatomical labeling atlas. *NeuroImage* **122**, 1–5 (2015).
62. Rolls, E. T., Huang, C.-C., Lin, C.-P., Feng, J. F. & Joliot, M. Automated anatomical labelling atlas 3. *NeuroImage* **206**, 116189 (2020).
63. Faul, F., Erdfelder, E., Lang, A.-G. & Buchner, A. G*Power 3: a flexible statistical power analysis program for the social, behavioral, and biomedical sciences. *Behav. Res. Methods* **39**, 175–191 (2007).
64. Tokuda, T. et al. Identification of depression subtypes and relevant brain regions using a data-driven approach. *Sci. Rep.* **8**, 14082 (2018).
65. Hawrylycz, M. J. et al. An anatomically comprehensive atlas of the adult human brain transcriptome. *Nature* **489**, 391–399 (2012).
66. Li, J. et al. Cortical structural differences in major depressive disorder correlate with cell type-specific transcriptional signatures. *Nat. Commun.* **12**, 1647 (2021).
67. Wang, L. B. et al. Association of structural measurements of brain reserve with motor progression in patients with Parkinson disease. *Neurology* **99**, E977–E988 (2022).
68. Allen Human Brain Atlas. *Allen Institute* <http://help.brain-map.org/display/humanbrain/Documentation> (2019).
69. French, L. & Paus, T. A FreeSurfer view of the cortical transcriptome generated from the Allen Human Brain Atlas. *Front. Neurosci.* **9**, 323 (2015).
70. Parkes, L., Fulcher, B. D., Yucel, M. & Fornito, A. Transcriptional signatures of connectomic subregions of the human striatum. *Genes Brain Behav.* **16**, 647–663 (2017).
71. Romme, I. A. C., de Reus, M. A., Ophoff, R. A., Kahn, R. S. & van den Heuvel, M. P. Connectome disconnectivity and cortical gene expression in patients with schizophrenia. *Biol. Psychiatry* **81**, 495–502 (2017).
72. Fulcher, B. D., Little, M. A. & Jones, N. S. Highly comparative time-series analysis: the empirical structure of time series and their methods. *J. R. Soc. Interface* **10**, 20130048 (2013).

Acknowledgements

This work received support from the following sources: STI2030-Major Projects (no. 2021ZD0200204 to J.Z.), National Key R and D Program of China (no. 2019YFA0709502 to J.F., no. 2019YFA0709501 to T.J., no. 2021YFC2500141 to T.J., no. 2022YFE012476 to T.J., no. 2018YFC1312900 to T.J. and no. 2018YFC1312904 to J.F.), Science and Technology Innovation 2030—Brain Science and Brain-Inspired Intelligence Project (no. 2022ZD0212800 to Y.J.), the National Natural Science Foundation of China (no. T2122005 to T.J., no. 82071997 to W.C., no. 82202242 to Y.J. and no. 81801773 to T.J.), the Shanghai Pujiang Project (no. 18PJ1400900 to T.J.), the 111 Project (no. B18015 to J.F.), the Shanghai Rising-Star Program (no. 21QA1408700 to W.C.), the China Postdoctoral Science Foundation (no. BX2021078 to Y.J. and no. 2021M700852 to Y.J.), the Shanghai Sailing Program from Shanghai Science and Technology Committee (no. 22YF1402800 to Y.J.), the key project of Shanghai Science and Technology (no. 16JC1420402 to J.F.), Shanghai Municipal Science and Technology Major Project (no. 2018SHZDZX01 to J.F.), ZJ Lab and Shanghai Center for Brain Science and Brain-Inspired Technology. This work is supported by the Zhangjing International Brain Biobank Consortium.

Author contributions

J.F. led the project. D.C., T.J., W.C. and J.F. were responsible for the study concept and the design of the study. V.V., X.W. and J.F. provided crucial advice for the study. D.C., Y.J., C.-Y.Z.L., L.W., C.S., S.X. and J.Z. analysed the data and created the figures. D.C. and V.V. wrote the manuscript. T.J. and W.C. made substantial contributions to the manuscript and provided critical comments. X.W., S.Y., W.C. and J.F. contributed to the data acquisition.

Competing interests

The authors declare no competing interests.

Additional information

Supplementary information The online version contains supplementary material available at <https://doi.org/10.1038/s44220-023-00139-4>.

Correspondence and requests for materials should be addressed to Tianye Jia, Wei Cheng or Jianfeng Feng.

Peer review information *Nature Mental Health* thanks Karl Friston, Thomas Nickl-Jockschat and the other, anonymous, reviewer(s) for their contribution to the peer review of this work.

Reprints and permissions information is available at www.nature.com/reprints.

Publisher's note Springer Nature remains neutral with regard to jurisdictional claims in published maps and institutional affiliations.

Springer Nature or its licensor (e.g. a society or other partner) holds exclusive rights to this article under a publishing agreement with the author(s) or other rightsholder(s); author

self-archiving of the accepted manuscript version of this article is solely governed by the terms of such publishing agreement and applicable law.

© The Author(s), under exclusive licence to Springer Nature America, Inc. 2023

ZIB Consortium

Di Chen^{1,2,13}, **Yuchao Jiang**^{1,2}, **Chun-Yi Zac Lo**^{1,2}, **Linbo Wang**^{1,2}, **Chun Shen**^{1,2}, **Shitong Xiang**^{1,2}, **Jie Zhang**^{1,2}, **Tianye Jia**^{1,2,7}, **Wei Cheng**^{1,2,8,9,10,11} & **Jianfeng Feng**^{1,2,12}

DIRECT Consortium

Xiang Wang^{3,4,5,13} & **Shuqiao Yao**³

Lists of members and their affiliations for the DIRECT Consortium appear in Supplementary Information.

Reporting Summary

Nature Portfolio wishes to improve the reproducibility of the work that we publish. This form provides structure for consistency and transparency in reporting. For further information on Nature Portfolio policies, see our [Editorial Policies](#) and the [Editorial Policy Checklist](#).

Statistics

For all statistical analyses, confirm that the following items are present in the figure legend, table legend, main text, or Methods section.

n/a Confirmed

- The exact sample size (n) for each experimental group/condition, given as a discrete number and unit of measurement
- A statement on whether measurements were taken from distinct samples or whether the same sample was measured repeatedly
- The statistical test(s) used AND whether they are one- or two-sided
Only common tests should be described solely by name; describe more complex techniques in the Methods section.
- A description of all covariates tested
- A description of any assumptions or corrections, such as tests of normality and adjustment for multiple comparisons
- A full description of the statistical parameters including central tendency (e.g. means) or other basic estimates (e.g. regression coefficient) AND variation (e.g. standard deviation) or associated estimates of uncertainty (e.g. confidence intervals)
- For null hypothesis testing, the test statistic (e.g. F , t , r) with confidence intervals, effect sizes, degrees of freedom and P value noted
Give P values as exact values whenever suitable.
- For Bayesian analysis, information on the choice of priors and Markov chain Monte Carlo settings
- For hierarchical and complex designs, identification of the appropriate level for tests and full reporting of outcomes
- Estimates of effect sizes (e.g. Cohen's d , Pearson's r), indicating how they were calculated

Our web collection on [statistics for biologists](#) contains articles on many of the points above.

Software and code

Policy information about [availability of computer code](#)

Data collection

Data analysis

For manuscripts utilizing custom algorithms or software that are central to the research but not yet described in published literature, software must be made available to editors and reviewers. We strongly encourage code deposition in a community repository (e.g. GitHub). See the Nature Portfolio [guidelines for submitting code & software](#) for further information.

Data

Policy information about [availability of data](#)

All manuscripts must include a [data availability statement](#). This statement should provide the following information, where applicable:

- Accession codes, unique identifiers, or web links for publicly available datasets
- A description of any restrictions on data availability
- For clinical datasets or third party data, please ensure that the statement adheres to our [policy](#)

The data of the AHBA microarray dataset is available from the website (<http://human.brain-map.org>). The data of REST-meta-MDD project from the DIRECT Consortium is available from the website (<http://www.rfmri.org/REST-meta-MDD>). The data from the Japan DecNef Project is available from the website (<https://bicr.atr.jp/decnefpro/>). The data from Second Xiangya Hospital within the ZIB Consortium is not available for public download, but access can be requested through the corresponding author J.F. (jffeng@fudan.edu.cn). Requests for raw and analyzed data will be promptly reviewed by the Fudan University ethics committee to verify whether the request is subject to any intellectual property or confidentiality obligations.

Human research participants

Policy information about [studies involving human research participants and Sex and Gender in Research](#).

Reporting on sex and gender

The self-reported 'sex' was used due to its biological attribution. The sex was regressed out as a covariate in our analyses.

Population characteristics

1151 MDD patients and 1064 healthy control (HC) individuals from the REST-meta-MDD consortium (age 37.21 ± 14.64 , 68% female for MDD; age 36.35 ± 15.53 , 60% female for HC) were included as the discovery dataset. For two replication datasets, the Japan DecNef Project (nMDD = 253, nHC = 585, age 42.49 ± 11.99 , 47% female for MDD; age 39.69 ± 15.48 , 55% female for HC; "<https://bicr.atr.jp/decnefpro/>") and the Second Xiangya Hospital study (nMDD = 385, nHC = 502, age 23.20 ± 6.42 , 68% female for MDD; age 21.45 ± 3.91 , 64% female for HC) were also investigated.

Recruitment

All individuals were recruited from multiple sites

Ethics oversight

Ethical permission was approved by the medical research ethics committee, and informed consent was obtained from all participants.

Note that full information on the approval of the study protocol must also be provided in the manuscript.

Field-specific reporting

Please select the one below that is the best fit for your research. If you are not sure, read the appropriate sections before making your selection.

Life sciences Behavioural & social sciences Ecological, evolutionary & environmental sciences

For a reference copy of the document with all sections, see [nature.com/documents/nr-reporting-summary-flat.pdf](https://www.nature.com/documents/nr-reporting-summary-flat.pdf)

Life sciences study design

All studies must disclose on these points even when the disclosure is negative.

Sample size

Due to the absence of a thorough exploration of comprehensive effect size or power calculation for SuStaln, we determined the sample size based on prior SuStaln investigations (Yuchao et al., 2023, Nature Mental Health; Young et al., 2018, Nature Communications; Vogel et al., 2021, Nature Medicine). These preceding studies suggested that approximately 30-40% of subjects would demonstrate measurable reductions in abnormal gray matter volume. Thus, it was imperative for us to analyze data from a minimum of 600 patients with MDD, and preferably exceeding 1000. We successfully achieved this objective.

Data exclusions

Outliers (MDD outlier ratio = $125/1276 = 9.80\%$, HC outlier ratio = $37/1104 = 3.35\%$ for the REST-meta-MDD consortium; MDD outlier ratio = $2/255 = 0.78\%$, HC outlier ratio = $13/598 = 2.17\%$ for the Japan DecNef Project; MDD outlier ratio = $14/400 = 3.50\%$, HC outlier ratio = $3/505 = 0.59\%$ for the Second Xiangya Hospital study) were identified if showing negative correlations with most of the rest of the individuals in terms of the whole brain structure patterns and hence removed.

Replication

To cross-validate our findings, we then confirmed that our observed subtypes from our discovery data were robust across two independent datasets. The SuStaln procedure with identical parameters was also conducted in two replication datasets from the Japan DecNef Project (253 patients with MDD, 585 healthy controls) and the Second Xiangya Hospital (385 patients with MDD, 502 healthy controls) respectively.

Randomization

This is not relevant because we did not conduct a controlled trial. Instead, we merged individuals with MDD from different cohorts and employed a data-driven algorithm for subtyping. Subsequently, we performed comparisons of demographic and disease characteristics across these subtypes.

Blinding

Blinding was not relevant for experiments because the SuStaln is a data-driven method without the need of demographic or clinical data. The individuals responsible for gathering demographic and clinical data were unaware of the SuStaln subtyping outcomes. Likewise, those

responsible for data preprocessing remained unaware of the demographic and clinical details. Thus, although the researchers were not personally blinded, the analysis itself remained effectively blinded.

Reporting for specific materials, systems and methods

We require information from authors about some types of materials, experimental systems and methods used in many studies. Here, indicate whether each material, system or method listed is relevant to your study. If you are not sure if a list item applies to your research, read the appropriate section before selecting a response.

Materials & experimental systems

- | n/a | Included in the study |
|-------------------------------------|--|
| <input checked="" type="checkbox"/> | <input type="checkbox"/> Antibodies |
| <input checked="" type="checkbox"/> | <input type="checkbox"/> Eukaryotic cell lines |
| <input checked="" type="checkbox"/> | <input type="checkbox"/> Palaeontology and archaeology |
| <input checked="" type="checkbox"/> | <input type="checkbox"/> Animals and other organisms |
| <input type="checkbox"/> | <input checked="" type="checkbox"/> Clinical data |
| <input checked="" type="checkbox"/> | <input type="checkbox"/> Dual use research of concern |

Methods

- | n/a | Included in the study |
|-------------------------------------|--|
| <input checked="" type="checkbox"/> | <input type="checkbox"/> ChIP-seq |
| <input checked="" type="checkbox"/> | <input type="checkbox"/> Flow cytometry |
| <input type="checkbox"/> | <input checked="" type="checkbox"/> MRI-based neuroimaging |

Clinical data

Policy information about [clinical studies](#)

All manuscripts should comply with the ICMJE [guidelines for publication of clinical research](#) and a completed [CONSORT checklist](#) must be included with all submissions.

- | | |
|-----------------------------|--|
| Clinical trial registration | the registered trial ID: ChiCTR2000031931 |
| Study protocol | Available online: https://www.chictr.org.cn/showproj.html?proj=51913 |
| Data collection | Clinical data were obtained through interviews, while brain imaging data were generated from MRI scanning sessions. Please refer to the Method section for more details. |
| Outcomes | The outcome is a clinical symptom assessed using the Hamilton Depression Rating Scale (HAMD). |

Magnetic resonance imaging

Experimental design

- | | |
|---------------------------------|-----|
| Design type | N/A |
| Design specifications | N/A |
| Behavioral performance measures | N/A |

Acquisition

- | | |
|-------------------------------|--|
| Imaging type(s) | Structural |
| Field strength | The field strength of the REST-meta-MDD project (http://www.rfmri.org/REST-meta-MDD), the Japan DecNef Project (https://bica.atr.jp/decnefpro/) are available from the official website. |
| Sequence & imaging parameters | The details of sequence parameters were provided in Methods. |
| Area of acquisition | Whole brain scan |
| Diffusion MRI | <input type="checkbox"/> Used <input checked="" type="checkbox"/> Not used |

Preprocessing

- | | |
|------------------------|---|
| Preprocessing software | Structural T1-weighted MRI brain scans were collected for each dataset. Using the VBM 8 toolbox (http://dbm.neuro.uni-jena.de/vbm8/), the office of the REST-meta-MDD consortium conducted standard preprocessing as reported in previous studies. Aligned with the REST-meta-MDD consortium, similar image preprocessing was conducted for the Japan DecNef Project and the Second Xiangya Hospital study, and briefly described as follows: we first segmented the structural T1-weighted MRI into gray matter (GM), white matter (WM), and cerebrospinal fluid (CSF) using a unified segmentation routine (http://www.neuro.uni-jena.de/vbm). We then employed the diffeomorphic anatomical registration through exponential lie (DARTEL) algebra tool to transform individual native space into standard montreal neurological institute (MNI) space with 1.5×1.5×1.5 mm resolution with an iterative registration. We modulated the gray matter maps by multiplying the linear and |
|------------------------|---|

	nonlinear components of the Jacobian determinants, resulting in GM images.
Normalization	Nonlinearly normalized to MNI space.
Normalization template	MNI space
Noise and artifact removal	N/A
Volume censoring	N/A

Statistical modeling & inference

Model type and settings	The SuStaln model was used to perform disease progression modeling.
Effect(s) tested	This is not relevant
Specify type of analysis:	<input type="checkbox"/> Whole brain <input type="checkbox"/> ROI-based <input checked="" type="checkbox"/> Both
Anatomical location(s)	Automated Anatomical Labeling Atlas
Statistic type for inference (See Eklund et al. 2016)	N/A
Correction	Either permutation, false discover rate correction and Bonferroni correction was applied wherever applicable.

Models & analysis

n/a	Involved in the study
<input checked="" type="checkbox"/>	<input type="checkbox"/> Functional and/or effective connectivity
<input checked="" type="checkbox"/>	<input type="checkbox"/> Graph analysis
<input checked="" type="checkbox"/>	<input type="checkbox"/> Multivariate modeling or predictive analysis